

Beam Test of a Prototype CsI Calorimeter

R.S. Kessler, A. Roodman, P. Shawhan, N. Solomey and B. Winstein

*University of Chicago
5640 S. Ellis Avenue, Chicago, Illinois 60637*

S. Hansen, H. Nguyen, R. Ray, R. Tschirhart and J. Whitmore

*Fermi National Accelerator Laboratory
P.O. Box 500, Batavia, Illinois 60510*

T. Nakaya

*Osaka University
Toyonaka, Osaka 560, Japan*

M. Lindgren

*University of California, Los Angeles
405 Hilgard Avenue, Los Angeles, California 90095-1547*

May 1995

Submitted to *Nuclear Instruments and Methods*

Disclaimer

This report was prepared as an account of work sponsored by an agency of the United States Government. Neither the United States Government nor any agency thereof, nor any of their employees, makes any warranty, expressed or implied, or assumes any legal liability or responsibility for the accuracy, completeness, or usefulness of any information, apparatus, product, or process disclosed, or represents that its use would not infringe privately owned rights. Reference herein to any specific commercial product, process, or service by trade name, trademark, manufacturer, or otherwise, does not necessarily constitute or imply its endorsement, recommendation, or favoring by the United States Government or any agency thereof. The views and opinions of authors expressed herein do not necessarily state or reflect those of the United States Government or any agency thereof.

Beam Test of a Prototype CsI Calorimeter

R.S.Kessler, A.Roodman, P.Shawhan, N.Solomey, B.Winstein,
University of Chicago, 5640 S. Ellis Ave, Chicago, Illinois 60637, USA.

S.Hansen, H.Nguyen, R.Ray, R.Tschirhart, J.Whitmore,
*Fermi National Accelerator Laboratory, P.O. Box 500, Batavia,
Illinois, 60510, USA.*

T.Nakaya
Department of Physics, Osaka University, Toyonaka, Osaka 560, Japan.

M.Lindgren
*University of California, Los Angeles, 405 Hilgard Ave.,
Los Angeles California, 90095-1547, USA.*

May 11, 1995

ABSTRACT

A prototype electromagnetic calorimeter for the KTeV experiment at Fermilab was tested at the CERN X1 beam-line. The calorimeter consisted of undoped cesium iodide crystals which were exposed to electrons, pions and muons. This test also featured a new digital readout system with 17 bits of dynamic range. The electron energy resolution is better than 1% at 5 GeV/c, and less than 0.5% at 60 GeV/c. The rejection factor for 40 GeV/c pions is estimated to be several hundred with 95% electron efficiency.

1 Introduction

The new KTeV detector at Fermilab is being constructed to measure the CP violating parameter $\text{Re}(\epsilon'/\epsilon)$ and to search for and study rare decays of neutral Kaons. This article will focus on the performance of a prototype of the KTeV cesium iodide calorimeter [1, 2], which is designed to accurately measure the energy and position of photons and electrons, and to distinguish pions from electrons.

The required performance of the KTeV electromagnetic calorimeter places stringent requirements on the shower medium, photomultiplier tubes, and the readout electronics. The design goal is to achieve 1% resolution for 15 GeV photons, and a non-linearity that does not exceed $\pm 0.5\%$ up to 80 GeV. In addition, the photomultiplier tubes and the readout electronics need to be sensitive to transverse cosmic muons which deposit ~ 30 MeV in a crystal; this necessitates ~ 1 MeV sensitivity at the low end of the dynamic range. The result is a requirement of 17 bits to cover the full operating range for the KTeV experiment. Since the calorimeter will ultimately operate in a high rate environment, the readout needs to provide information on the time structure of the photomultiplier tube pulses. To meet these requirements, a pure CsI crystal calorimeter was chosen, and the digital readout system was designed to operate at high frequency with a wide dynamic range.

A 25 channel CsI prototype was exposed to a test beam at CERN in August, 1994. The goals of this calorimeter test were to measure its energy resolution, its ability to distinguish charged pions from electrons, and to measure the light collection uniformity using transverse muons. The absolute energy scale was not studied because of uncertainties in the beam momentum and because of temperature fluctuations which changed the CsI response. The organization of this article is as follows. The experimental setup at CERN is discussed in Sec. 2. In Sec. 3, results are presented on the calibration and on the electron energy resolution between 5 and 60 GeV/c. The pion/electron separation at 40 GeV is discussed in Sec. 4, and an *in-situ* uniformity measurement using transverse beam muons is described in Sec. 5. The Monte Carlo simulations are described in Sec. 6.

2 Experimental Setup

The experiment took place at the X1 beam-line of the CERN SPS. The experimental setup is shown in Fig. 1. The prototype calorimeter consisted of 25 CsI crystals arranged in a 5×5 array. The digital readout system was located several inches behind the PMTs. The CsI crystals and readout electronics were enclosed in an aluminum box. At the upstream face of the box was a beam entrance window made of two sheets of black paper and mylar. The sections below give further details about the various components in the setup.

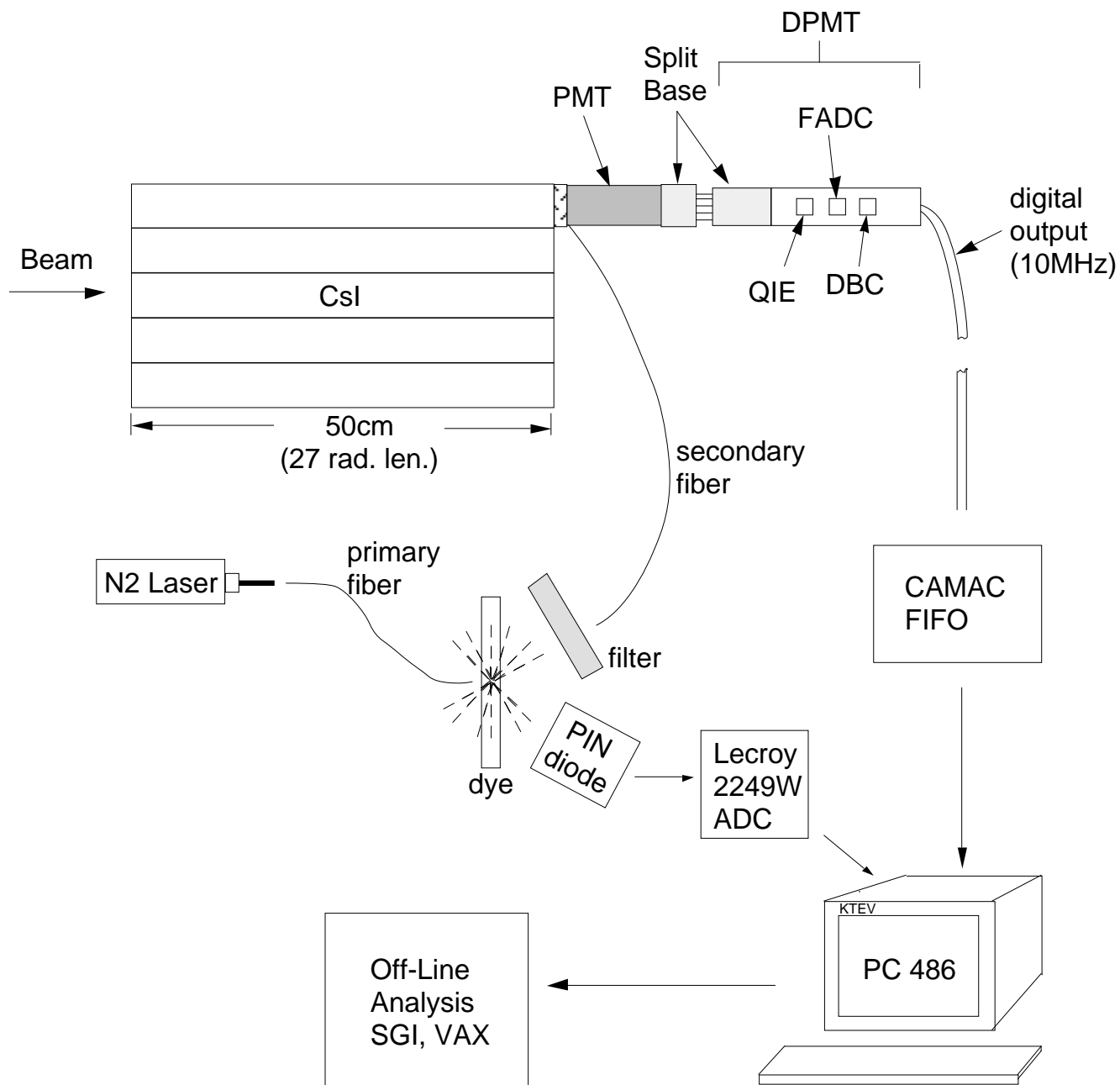


Figure 1: Experimental setup for CERN beam test.

2.1 CsI Crystals

Undoped cesium iodide was chosen for the KTeV calorimeter because of its fast scintillation response and relatively high resistance to radiation damage. Nineteen of the crystals were produced by Crismatec, and the remaining six were produced by Horiba. The Crismatec crystals consisted of two halves glued together with Epo-Tek 305 epoxy, which was chosen for its high UV transmission. The measured transverse dimensions of the crystals were within ± 0.1 mm of the nominal size of 50 mm. The crystal lengths were 500 ± 1 mm (27 radiation lengths).

The crystals were wrapped with 12 micron thick opaque mylar. The upstream section of the mylar wrapping was aluminized, and the downstream section was black. The location of the boundary between the aluminized and black mylar sections was tuned for each crystal such that the light collection efficiency was nearly uniform along the length of the crystal. The resulting non-uniformities were typically several percent, which reduced the sensitivity of the energy measurement to fluctuations in the longitudinal shower development.

The contribution from photo-statistics to the energy resolution was less than 0.3% for the energies of interest. Between 80 and 90% of the scintillation light is collected within a 100ns gate. The scintillation spectrum can be approximately characterized by a ‘fast’ and a ‘slow’ component. The fast light spectrum peaks at 315nm and has a time constant of ~ 20 ns; the slow light spectrum is peaked near 420nm and has a time constant of $\sim 1\mu$ s.

The temperature dependence of the CsI light yield is about -1.5% per degree Celsius. Since we had no temperature control inside the CsI box, we monitored the air temperature at each corner of the CsI array with AD590 thermo-sensors, which were sensitive to changes at the level of $\sim 0.1^\circ\text{C}$. We observed temperature changes of a few degrees between night and day and thus had to correct the CsI response as a function of time.

2.2 CsI Photomultiplier Tubes

Each crystal was viewed by a six-stage 1.5” R5330 Hamamatsu photomultiplier tube (PMT). The PMTs are linear in their response to within $\pm 0.5\%$ for peak anode currents up to 15mA. The front face of the PMT is made of UV-transmitting glass to accomodate the emission spectrum of the fast scintillation light from the CsI crystals. The PMTs were wrapped with two layers of 0.002 inch kapton, with one layer of 0.005 inch mu-metal in between. The mu-metal served as an RF shield, and shared a common ground with the anode and dynode signals produced by the PMT. Another layer of 0.020 inch mu-metal surrounded the last kapton layer, and was separated from the kapton with insulating spacers.

The PMTs were coupled to the crystals with two layers of 5mm thick General Electric RTV 656. Between the two RTV ‘cookie’ layers was a 1mm thick Schott UG 11 glass filter. This filter has good transmission for the fast UV scintillation light, while absorbing most of the slow light which is produced at longer wavelengths. Light yields of 20–40 photo-electrons per MeV were obtained from the crystals with this configuration. The PMTs were held in place with springs that applied pressure to the socket assembly.

2.3 CsI Readout Electronics

An innovative readout technology was used to digitize photomultiplier tube signals from the calorimeter [3, 4, 5]. The major components of this digital photomultiplier tube base (DPMT) are a high voltage divider for the photomultiplier tube, a charge integrating and encoding (QIE) custom integrated circuit, an Analog Devices AD9002 8-bit FADC and a driver/buffer/clocking (DBC) custom integrated circuit. The primary features of the digitizer are shown in Figure 2. The system operated at 10 MHz, corresponding to a 100 ns clock cycle, and spanned 17 bits of dynamic range.

The DPMT has nine non-overlapping sensitivity ranges. For each clock cycle it produces a 12-bit floating point number; an 8-bit mantissa and a 4-bit exponent. For a given input current integrated over a clock cycle, the QIE selects the appropriate sensitivity range and sends a voltage to the 8-bit FADC. The sensitivity range is encoded as the 4-bit exponent while the output from the FADC forms the 8-bit mantissa. The sensitivity range parameters are shown in Table 1.

The operation of the digitizing circuit is shown in Figure 3. The crucial component of the DPMT is the QIE,¹ which adds a fixed bias current to the PMT anode signal current, divides the total current into nine binary ranges ($I/2$, $I/4$, $I/8$, ... $I/512$), and simultaneously integrates the divided currents on nine separate 1 pF capacitors. The nine capacitor voltages are then compared to a common reference voltage. The result of this comparison is used to form the 4-bit exponent and to select the capacitor which will send its voltage to the FADC.

The QIE operations are pipelined, with four identical circuits functioning in a round-robin fashion. The duration of each operation is one clock cycle. Each QIE has a total of 36 capacitors, with four capacitors per range. To label the first capacitor in the pipeline, the QIE generates a capacitor identification bit every fourth clock cycle.

The DBC chip synchronizes the mantissa and exponent information. For each clock cycle, the 12-bit floating point output and the capacitor ID bit were transferred into a custom built CAMAC data buffer. Upon receipt of a trigger, the digital information was held in the data buffer until readout.

The power dissipation of the DPMT was 4.0 watts, of which 0.5 watts were due to the HV divider. Since the CsI response is sensitive to temperature, the PMT base was split to help isolate the crystals from the heat generated by the readout electronics. The upstream socket assembly (see Fig. 2) includes the PMT socket and the bypass capacitors. The HV divider contains the heat generating elements of the base and was located 6" downstream of the PMT. A bundle of thin wires carried the dynode and cathode voltages from the HV divider to the PMT. The anode and dynode signals were carried by RG178 coaxial cables.

¹The concept behind the QIE was originally developed for the SDC experiment.

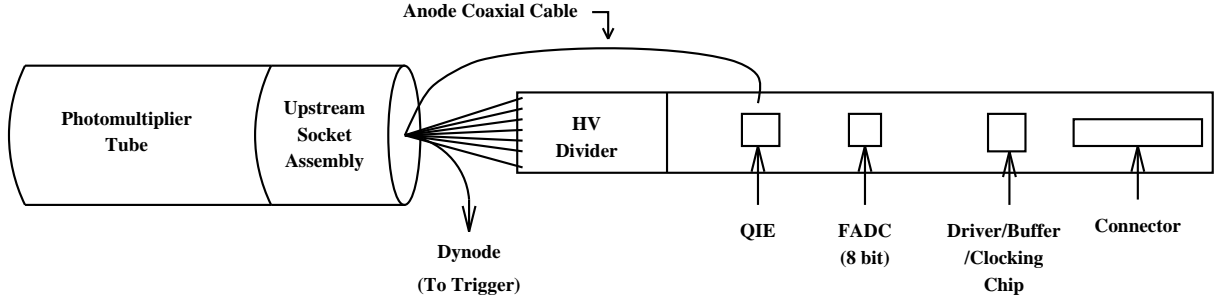


Figure 2: Illustration of the base and DPMT card. The DPMT base incorporates both the PMT high voltage divider and the digital readout circuit. Drawing is not to scale.

Table 1: Dynamic range of QIE digitizing circuit.

Range	current split	Charge		Energy	
		(in range,pC)	(fC/count)	(in range,MeV)	(MeV/count)
2	I/2	0-2	13	0-200	1
3	I/4	2-6	26	200-600	2
4	I/8	6-14	51	600-1400	4
5	I/16	14-30	103	1400-3000	8
6	I/32	30-62	205	3000-6200	16
7	I/64	62-126	410	6200-12600	32
8	I/128	126-254	820	12600-25400	64
9	I/256	254-510	1640	25400-51000	128
10	I/512	510-1022	3280	51000-102200	256

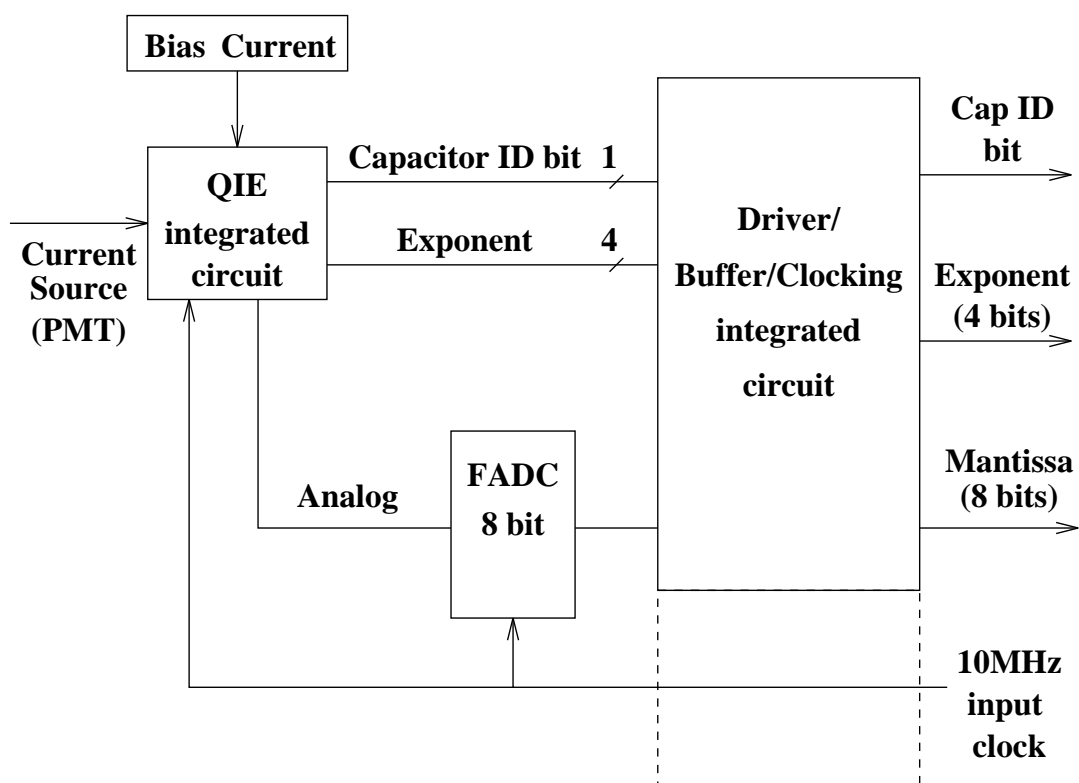


Figure 3: A block diagram of the operation of the digitizing base.

2.4 Laser Calibration System

The calibration of the nine-range DPMT system was performed with a specially designed laser/dye system that injected a measured amount of light into each PMT. Each crystal was attached to a quartz fiber that delivered pulses of light from a laser/dye system (Fig. 1). The amplitude of each pulse was monitored independently by two PIN photodiodes, so that the FADC and range values could be related to the PIN photodiode signal. A laser calibration run consisted of varying the light pulse intensity over most of the dynamic range of the DPMT. Further details about the laser calibration hardware are given below, while the calibration procedure is discussed in Sec. 3.1.

The system was driven by a Laser Science VSL337-ND Nitrogen laser running between 1 and 5 Hz in pulsed mode. The maximum laser output was 250 microjoules per pulse, and the rms output fluctuation was about 7%. Laser light was focused onto a 1 mm core diameter fiber. This primary fiber transmitted the laser light onto a liquid dye. The input end of this primary fiber could be moved in and out of the laser beam, so that the intensity of light onto the liquid dye could be varied.

The liquid dye served to reemit the light isotropically and to convert the time profile of the laser pulse into a pulse that is similar to the CsI pulse shape. The dye was a solution of sodium salicylate dissolved in ethanol, and was contained in a rectangular quartz cuvette. The concentration was such that the dye absorption length was 2 cm at 337 nm, which is the Nitrogen laser output wavelength. The 10-90% rise and fall times of the dye pulse shape were approximately 3 and 13 nsec respectively.

The pulsed light from the dye was fed to each PMT via a 2.5 meter long, 1 mm core diameter quartz optical fiber. Each of these 25 secondary fibers viewed the liquid dye light source from a distance of approximately 4 cm. The output ends of these fibers terminated at the downstream end of the crystals; light exiting from the fibers entered the PMT cathodes primarily by reflection from the upstream surface of the crystals. A set of neutral density filters was placed between the liquid dye and the secondary fibers. By moving the primary fiber in and out of the laser beam, and by selecting filters with different transmissions, the light level could be adjusted to cover most of the dynamic range of the digital readout system.

Also viewing the pulsed light from the liquid dye were two Hamamatsu R1722-02 PIN photodiodes. The output of the PIN photodiodes were digitized by a LeCroy 2249W ADC.

2.5 The X1 Beam-Line

The CERN X1 beam-line [6] was used to deliver electrons, pions, and muons to the prototype CsI calorimeter. The X1 beam-line is a tertiary beam derived from a 120 GeV/c negative secondary beam. The secondary beam consists mostly of electrons and pions. Electrons were produced in the X1 beam-line using a Pb target without any further absorber. Pions were produced from a Cu target with an absorber, and muons were produced from a 70 GeV/c pion beam incident on closed collimators.

For the electron data samples, the collimation in the beam-line was set to minimize the momentum dispersion of the beam. The average rate for the optimized beam tune was about 1 Hz. Material in the beam-line, such as scintillator and Cerenkov gas, was removed to further minimize momentum dispersion and multiple scattering. The result was an extremely pure electron beam with a predicted momentum dispersion of 0.44% at 20 GeV/c. The beam transport calculations were made using the program TURTLE[7, 8] which does not simulate radiative processes in the tertiary

beam-line, and hence may underestimate the momentum dispersion. Figure 4 shows the predicted dispersion as a function of electron momenta from 5 to 60 GeV/c.

High statistics were required to study pion rejection in the calorimeter, so the collimators were opened. This resulted in an average rate of 10Hz and a 2.5% RMS momentum dispersion for the 40 GeV/c pions and electrons used in this study.

A 70 GeV/c pion beam incident on closed collimators was used to generate muons with an average rate of about 0.01 Hz/cm².

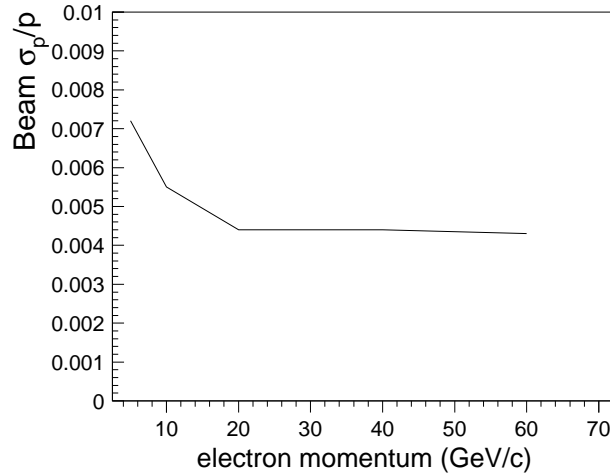


Figure 4: The predicted momentum dispersion vs. electron momentum in the X1 beam-line at CERN.

2.6 Trigger

The electron data were triggered on the the sum of dynode signals from the central nine crystals. This allowed us to remove the trigger-scintillators from the beam-line and thus minimize the amount of material in front of the CsI. The threshold on the dynode-sum required that the energy deposit in the central nine crystals exceeded 25% of the beam energy. All of the data were taken asynchronously with respect to the phase of the 10MHz clock that drives the digital readout system. The arrival time of the beam particle with respect to the clock phase was measured with a LeCroy 2228 TDC.

For the pion and muon studies, a dynode-sum trigger would have rejected minimum ionizing particles; we triggered instead on a coincidence of signals from scintillation counters in the beam-line.

3 Electron Data

The primary goal of this beam test was to measure the energy resolution of the prototype CsI calorimeter. To this end, most of the six day beam test was devoted to accumulating electron data.

To study the calorimeter resolution, an electron *energy scan* was performed with electrons ranging in momenta from 5 to 60 GeV/c, incident on the center block of the array. To calibrate the energy response of the central nine crystals, the beam momentum was fixed at 20 GeV/c, and the array was moved so that electrons were incident on each of the central nine CsI crystals. The illumination resulting from the *position scan* is shown in Fig. 5. The beam spot size at the CsI face was roughly 3.3 cm by 1.3 cm (FWHM), and was positioned approximately in the center of each crystal. The CsI energy deposits were used to reconstruct the electron position by calculating the ratio between energy in the central row or column and the energy in the adjacent row or column, and then comparing the results to a Monte Carlo prediction. From the Monte Carlo simulation, the expected position resolution at 20 GeV/c is ~ 1.4 mm.

The pedestal distribution is shown in Fig. 6 for a single channel, the sum of 9 channels, and the sum of 25 channels. The typical pedestal sigma is ~ 0.7 MeV. For the 9 channel sum, the fit sigma is 1.7 MeV, and there is a small non-Gaussian shoulder. For the 25 channel sum, the fit sigma is 3.5 MeV, and there is distinct bump 20 MeV from the central pedestal peak. The second peak in the pedestal distribution was from coherent noise that occasionally shifted the pedestal by ~ 0.8 MeV in every channel of the array. This pedestal shift is barely visible in a single channel, but becomes more pronounced when more channels are added. The origin of this noise is not known, but it was also correlated with pedestal shifts in the scintillator ADC channels. Since a 20 MeV shift is very small compared with the electron beam energies, the pedestal shifts were not corrected or removed from the data.

Figure 7 shows the raw FADC and range distributions in the central block for a 20 GeV/c electron beam. Most of the data lie in the lower end of range 8 [clear] and the upper end of range 7 [shaded]. The width of the response is due mainly to the finite spot size of the beam, so that a varying fraction of the electron energy is deposited in the central crystal. The FADC tail in ranges 6 and 7 is from scattered electrons, and from the small pion contamination in the electron beam. Note that the dynode-sum trigger prevents the lower ranges from being populated.

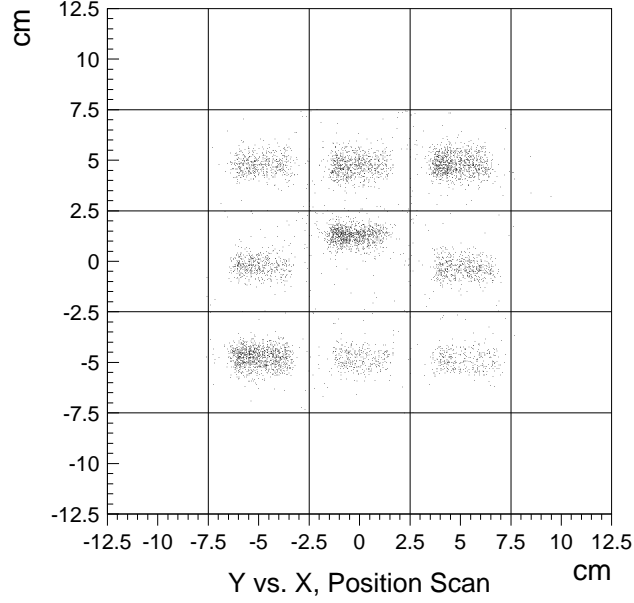


Figure 5: Position scan illumination at 20 GeV/c used for the energy calibration of each block.

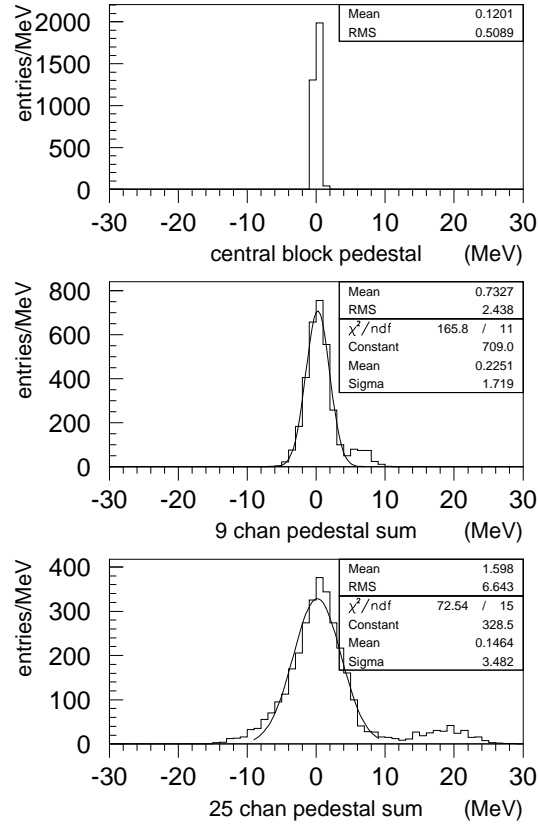


Figure 6: Pedestal distributions for the central block, the sum of the inner nine blocks, and the sum over all 25 blocks. These plots are for one of the four QIE capacitors.

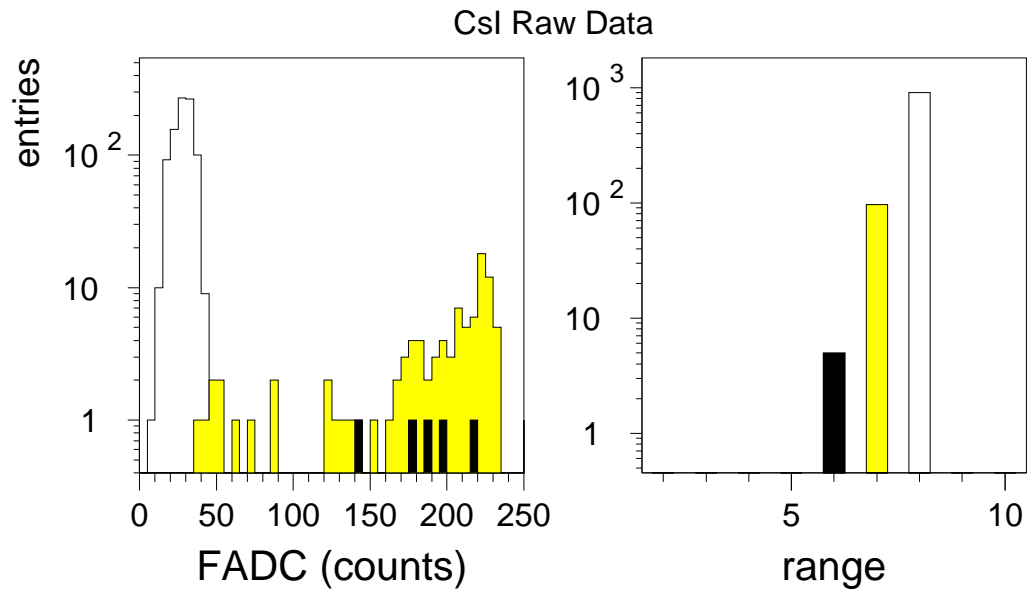


Figure 7: FADC and range distributions for the central block in the array, with a 20 GeV/c electron beam incident on the center block. The solid, grey and clear shadings correspond to ranges 6,7 and 8, respectively.

3.1 Calorimeter Calibration

The calibration procedure was broken into two independent steps. The first step was to determine the relationship between the digital output and the charge. The second step was to relate the charge to the energy deposited in each of the 25 blocks.

The conversion of mantissa and exponent values into charge was determined with data from the laser calibration system described in Sec. 2.4. At the end of taking data with the beam, several laser-scan runs were taken in which the light intensity of the dye was varied to scan the dynamic range of the digital readout. During these runs, the nine DPMT ranges were populated as uniformly as possible.

The number of FADC counts for the center block of the array is plotted against the PIN diode ADC counts in Fig. 8a for four of the nine sensitivity ranges. The other ranges were populated by inserting different filters between the dye and the secondary fibers. As the input charge increases, the FADC value increases to the top of the range, and then falls to the bottom of the next range. The calibration consisted of fitting a straight line to the FADC vs. PIN diode ADC counts in each range. The linear fits were done independently for the four capacitors in each range. The total number of parameters for the four capacitors and nine ranges is 72; thus for the 25 block array, there were 1800 calibration parameters. Figure 8b shows the charge measured by the DPMT vs. PIN diode ADC counts for the four sensitivity ranges after the fitting procedure. The straight line shows that the linear fits work very well.

The position scan data (see Fig. 5) were used to relate the measured charge in each block to the energy deposit. After converting the mantissa and exponent values to a charge Q_i , the energy deposit in block i is given by $E_i = g_i Q_i$. The energy calibration constants g_i were determined by minimizing the quantity

$$\chi^2 = \sum_{events} \left(\sum_{crystals} (g_i Q_i) - p \right)^2, \quad (1)$$

where $p = 20$ GeV/c was the electron momentum for all of the position scan data. The sum over crystals in eq. 1 refers to the nine blocks surrounding the block with the maximum energy deposit.

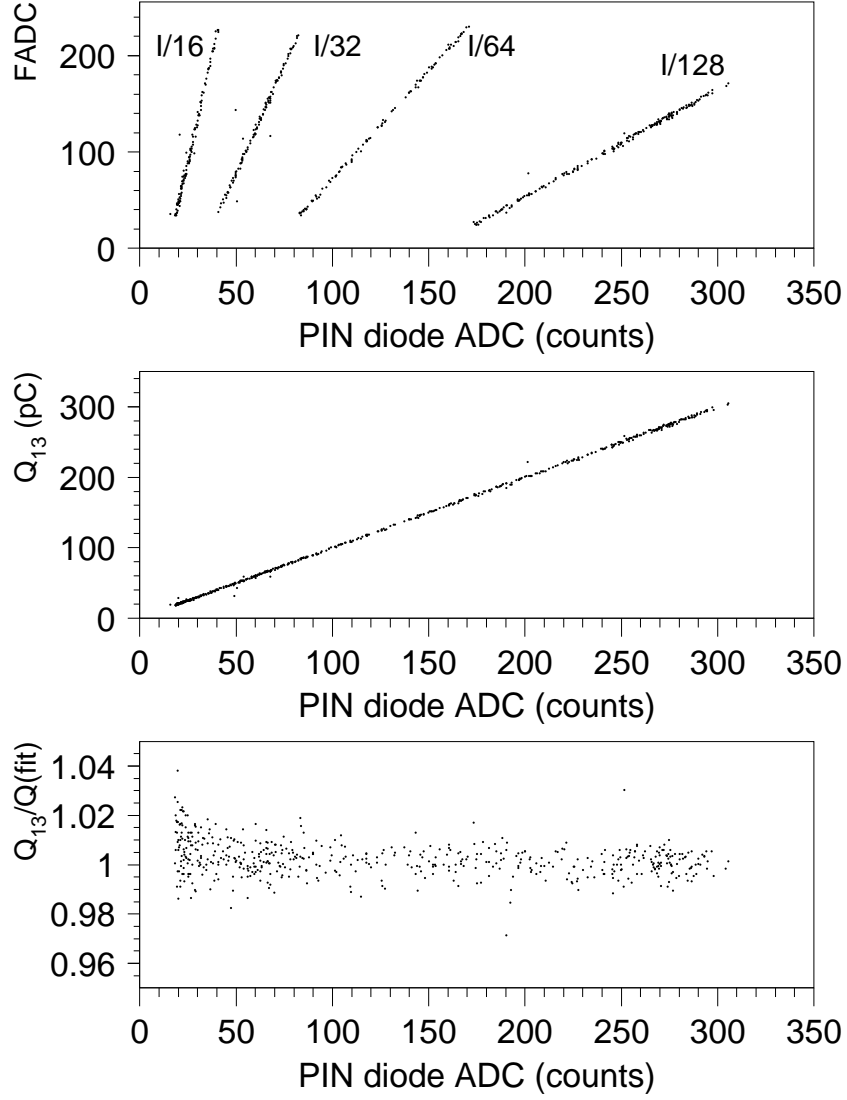


Figure 8: (a) The FADC values for the central block are plotted against the PIN diode ADC values. (b) the reconstructed DPMT charge Q_{13} for the central block is plotted against the PIN diode ADC values. (c) The ratio of reconstructed DPMT charge to the charge calculated from the fit is plotted against PIN diode ADC counts.

3.2 Analysis and Results

The reconstruction of electron energies was quite straightforward. The crystal with the maximum energy was found, and then the energy was summed in a 3×3 and 5×5 region around this crystal. In terms of the calibration constants g_i and the measured charges Q_i , we define

$$E(3 \times 3) \equiv \sum_{3 \times 3} g_i Q_i, \quad E(5 \times 5) \equiv \sum_{5 \times 5} g_i Q_i \quad (2)$$

to be the energy sum of 9 and 25 blocks, respectively. Note that the center crystal in the 3×3 sum is not necessarily the center block in the array. The energy in each block was determined from the charge measured in a single DPMT clock cycle. Once the individual block energies have been summed, some corrections were applied to obtain the final value for the energy deposited in the calorimeter. These corrections are described below.

Events were selected for analysis if their arrival time with respect to the beginning of the clock cycle, t_e , was between 8 and 18 ns. A linear correction was applied to the measured energy as a function of the arrival time t_e . This correction was determined from the data and is shown in Fig. 9 for 60 GeV/c electrons.

The temperature of the CsI array varied by $\sim 3.5^\circ\text{C}$ over the course of the energy scan and was observed to be correlated with changes in the mean E/p value. The temperature and E/p variation as a function of time are shown in Figs. 10a,b. The correlation between E/p and temperature is evident in Fig. 10c, although changes in E/p seem to lag changes in the temperature by about 0.1 days. This time lag may be due to the fact that the temperature of the air surrounding the CsI was measured, rather than the temperature of the CsI itself. To correct for this effect, the E/p spectrum at each energy was corrected linearly as a function of time. The linear fit used to correct 60 GeV/c electron data is shown in Fig. 11. A fit to the data in Fig. 10c indicates a 1.6% decrease in light output per 1 degree C increase in temperature; this agrees well with previous measurements.²

The E/p distributions for the electron energy scan are shown in Fig. 12, for 5, 10, 20, 30, 40, and 60 GeV/c electrons. Each spectrum is fit to a Gaussian distribution to determine the resolution. The spectra have been corrected for temperature and for the arrival time within the clock cycle. The measured E/p distributions have significant low side tails near $E/p \sim 0.98$, which are not reproduced by a beam transport simulation. The tails in the E/p distributions are most likely due to scattering and radiative effects in the beam-line [8]. Since radiative processes are not included in the beam transport program, the simulation is not expected to reproduce the low side tails observed in the data. The flat tail extending well below $E/p < 1$ is from the small pion contamination in the electron beam and from electrons that scattered upstream of the CsI.

The fitted $\sigma_{E/p}$ as a function of electron momentum is shown in Figs. 13a,b, along with predictions from a GEANT-based Monte Carlo[10]. At higher momenta, the resolution is dominated by the beam dispersion. If we take the calculation of the electron beam momentum spread at face value, we can infer the intrinsic resolution of the CsI prototype. Figures 13c,d show the inferred CsI resolution (for 5×5 and 3×3 sums) as a function of momentum, along with the GEANT-based Monte-Carlo predictions.

²A measurement at FNAL resulted in a temperature coefficient of $-1.4\%/^\circ\text{C}$, while another group measured $-1.5\%/^\circ\text{C}$ [9]

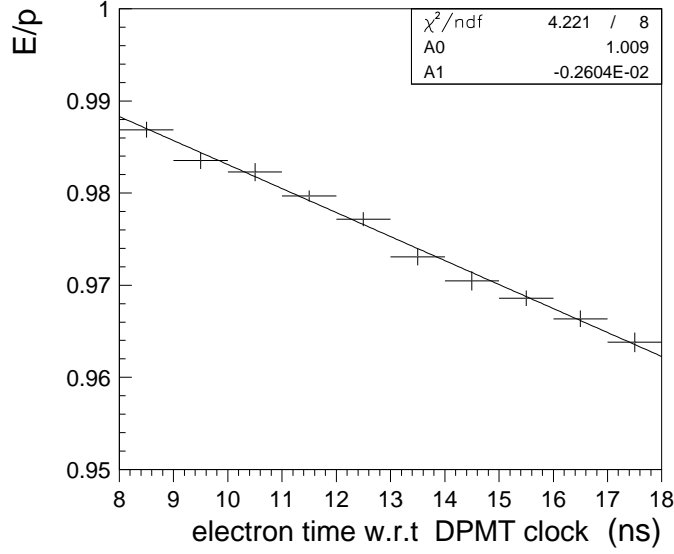


Figure 9: Reconstructed E/p vs. the electron arrival time t_e .

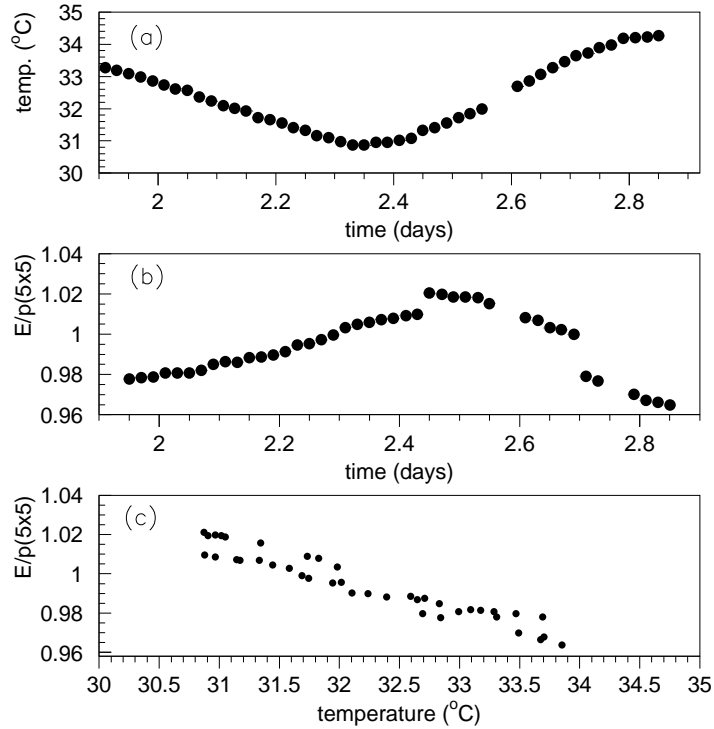


Figure 10: (a) The temperature of the air around the CsI crystals vs. time, (b) The mean of the measured E/p distributions vs. time. Note that the mean E/p value increases as the temperature decreases, and that the phase lag is about 0.1 days. (c) The mean of the measured E/p distributions vs. temperature. The E/p values are plotted for all of the energy scan data (5–60 GeV/c) before applying temperature corrections.

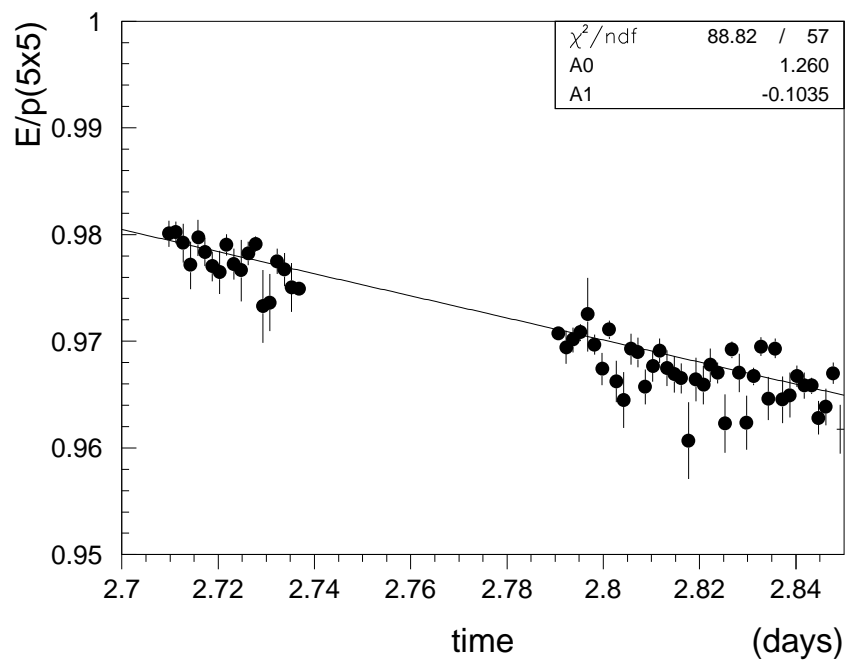


Figure 11: The mean of the E/p distribution vs. time for 60 GeV/c electron data.

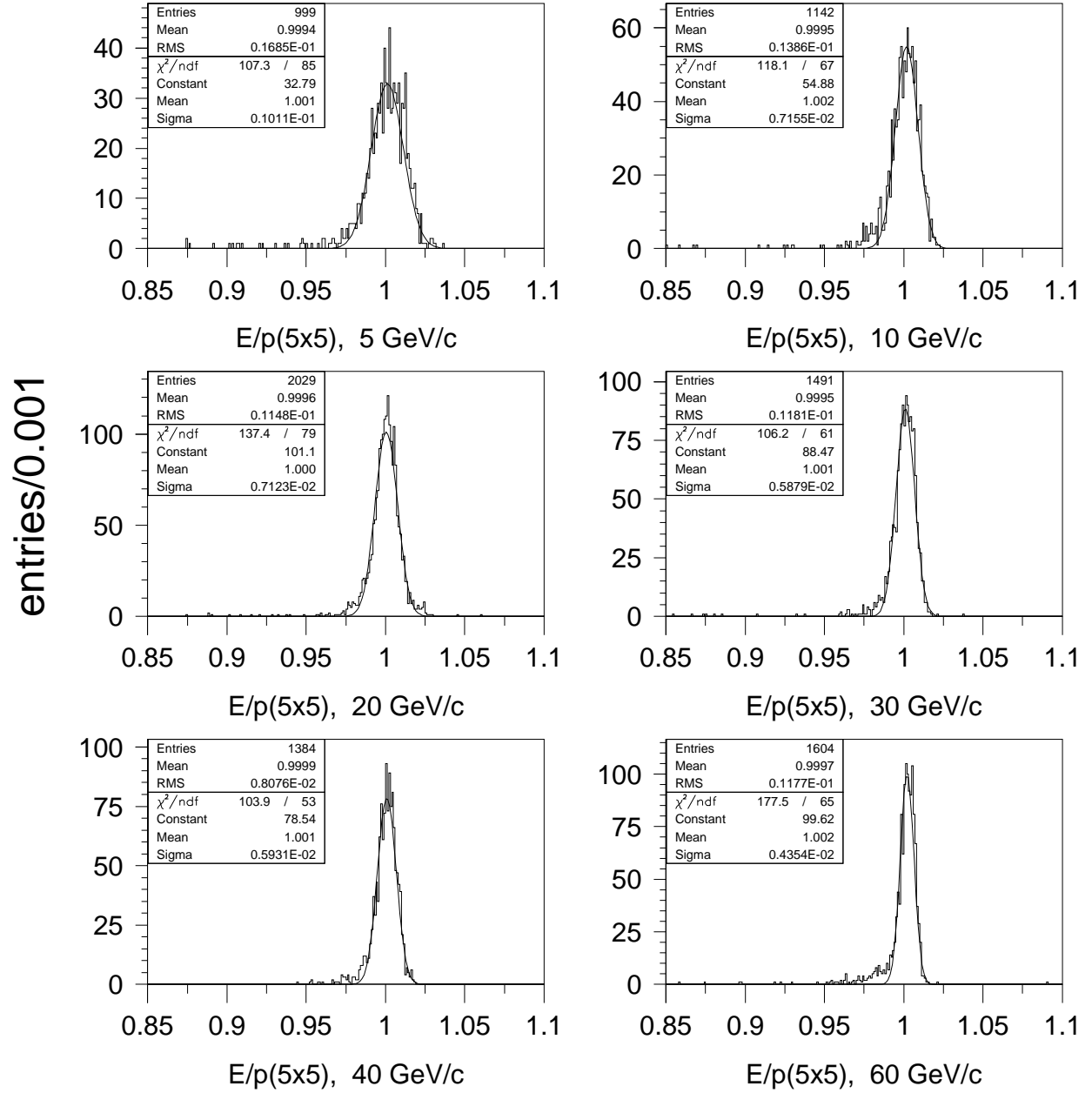


Figure 12: E/p spectra for 5,10,20,30,40 and 60 GeV/c electrons. Each spectrum has been corrected for the arrival time t_e in the DPMT slice, and for the ambient temperature variation during the run.

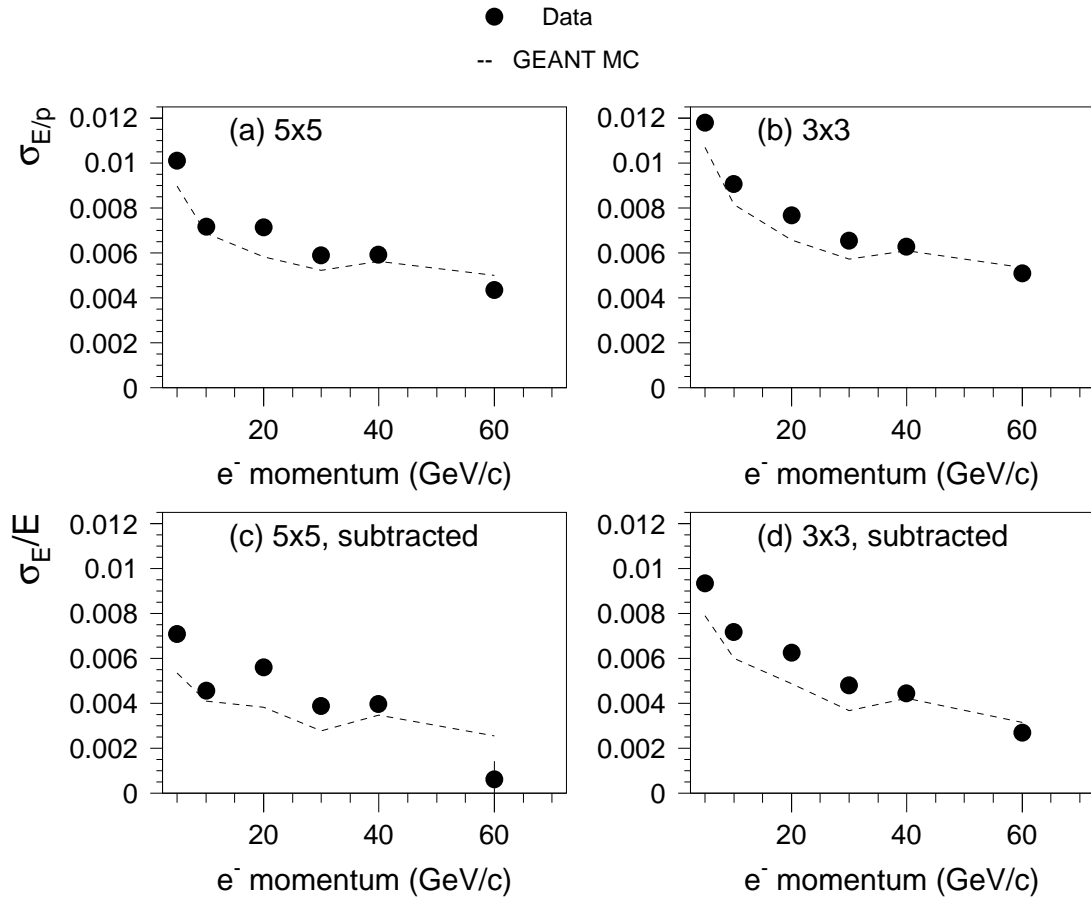


Figure 13: Resolution of E/p vs. p obtained from Gaussian fits for (a) 5x5 sum and (b) 3x3 sum. The intrinsic energy resolution with beam dispersion subtracted for (c) 5x5 sum and (d) 3x3 sum.

To illustrate the usefulness of the digital readout system in a high rate environment, the time structure of the CsI response is shown in Fig. 14 for a 40 GeV/c electron beam. The events in Fig. 14 arrived between 8 and 18 ns with respect to the beginning of a clock cycle. Clock cycle 5 (slice 5) is the in-time slice in which most of the fast scintillation light is produced. The early slices show pedestal fluctuations. The enhancement in slices 3 and 4 was due to internal QIE cross-talk. This cross-talk has been eliminated in later versions of the QIE. The late slices (after slice 5) show the slow time component of the CsI pulse shape. The bump around slice 16, which is about 1 micro-second after the signal, was due to PMT after-pulsing. The time profile in Fig. 14 was also measured for pions and muons, and was always observed to have the same shape. The after-pulse bump at slice 16 can even be seen for transverse muons that deposit 30 MeV (several hundred photo-electrons).

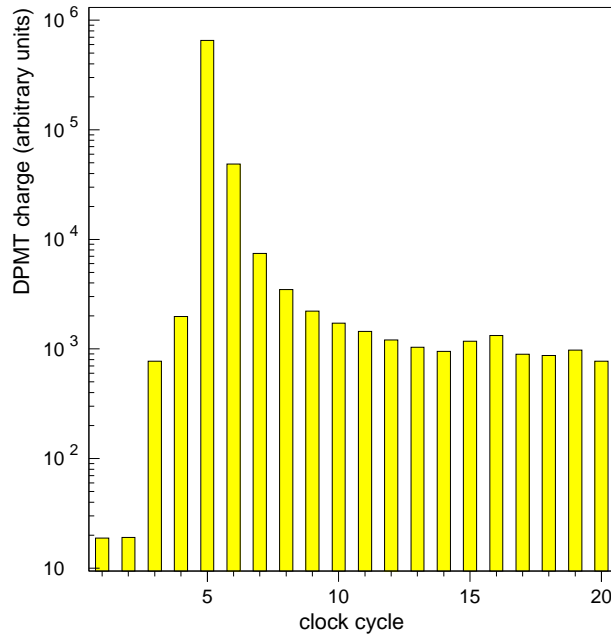


Figure 14: CsI time structure for 40 GeV e^- incident on the CsI calorimeter. The horizontal axis is the clock cycle, and is 100 ns per bin. The vertical axis is the DPMT charge summed over the entire run. This plot is for the central block only.

4 Electron/Pion Separation

An important requirement of the KTeV detector is to distinguish pions from electrons. For this reason, we measured the response of the calorimeter to both π^- and e^- beams at 40 GeV/c. High statistics were needed for this measurement, so the collimators were opened. This resulted in an average rate of ~ 10 Hz and a 2.5% RMS momentum spread. To select particle type, only the secondary targets were changed. Identical beam optics for both pions and electrons allowed for accurate comparisons of the energy distributions.

The pion and electron E/p spectra are shown in Fig. 15a, where the total energy was determined from the central 9 blocks. For the 40 GeV/c electron data, the e^- efficiency is taken to be 100% at $E/p = 0.9$; the E/p region below 0.9 was due mainly to a small pion contamination, and from electrons that scattered in the beam-line. As the E/p cut is moved above 0.9, the e^- efficiency drops and the π^- rejection increases. Fig. 16 shows the π^- rejection as a function of the e^- efficiency. For an e^- efficiency of 95%, the π^- rejection is $420 \pm 35(stat)$ at 40 GeV/c. Since the electron E/p resolution was dominated by the 2.5% RMS momentum spread of the beam, the separation of pions from electrons is underestimated. Using a more realistic width of 1% for the electron E/p distribution, the pion rejection factor increases to $720 \pm 75(stat)$ with 95% e^- efficiency (Fig. 16).

Fig. 15b shows the detailed MIP structure of the π^- energy deposition in the calorimeter. This illustrates the large dynamic range of digital readout system. The readout is actually sensitive to a few MeV, as demonstrated by the observation of transverse muon signals (next section).

The muon contamination of the pion beam was estimated by looking at energy deposits in the CsI blocks outside the central block where the pion beam was centered. Assuming that the muon halo was distributed uniformly over the array, it is estimated that the muon contamination was no more than a few percent of the pion beam. Unfortunately, we have no way to measure the e^- contamination of the pion beam; even a small contamination would make our pion rejection estimates too low. Thus we make a conservative estimate of the π/e separation by not correcting for electron contamination. There is no correction for muon contamination either, so the rejection may be a few percent too high if there was no electron contamination in the π^- beam.

A Monte Carlo simulation of a 40 GeV/c π^- beam incident on the CsI array was performed using GEANT/FLUKA [10]. The resulting E/p spectrum is compared with data in Fig. 17, which shows the MC/data ratio as a function of E/p . At $E/p \sim 1$ the Monte Carlo spectrum shows a deficit relative to the data, suggesting that there may be a small e^- contamination in the pion beam. The first two bins near $E/p \sim 0$ correspond to the MIP structure; the discrepancy reflects a disagreement of 30 MeV in the MIP peak value between data and Monte Carlo.

We next changed the beam polarity to get 40 GeV/c π^+ . The E/p spectra for π^- and π^+ are compared in Figs. 18a,b. The two spectra are seen to be very similar, except perhaps near $E/p \sim 1$. However, since the electron and positron contaminations are not known, it is difficult to compare the shapes near the E/p endpoint. Fig. 18c shows the π^-/π^+ ratio predicted by the Monte Carlo simulation.

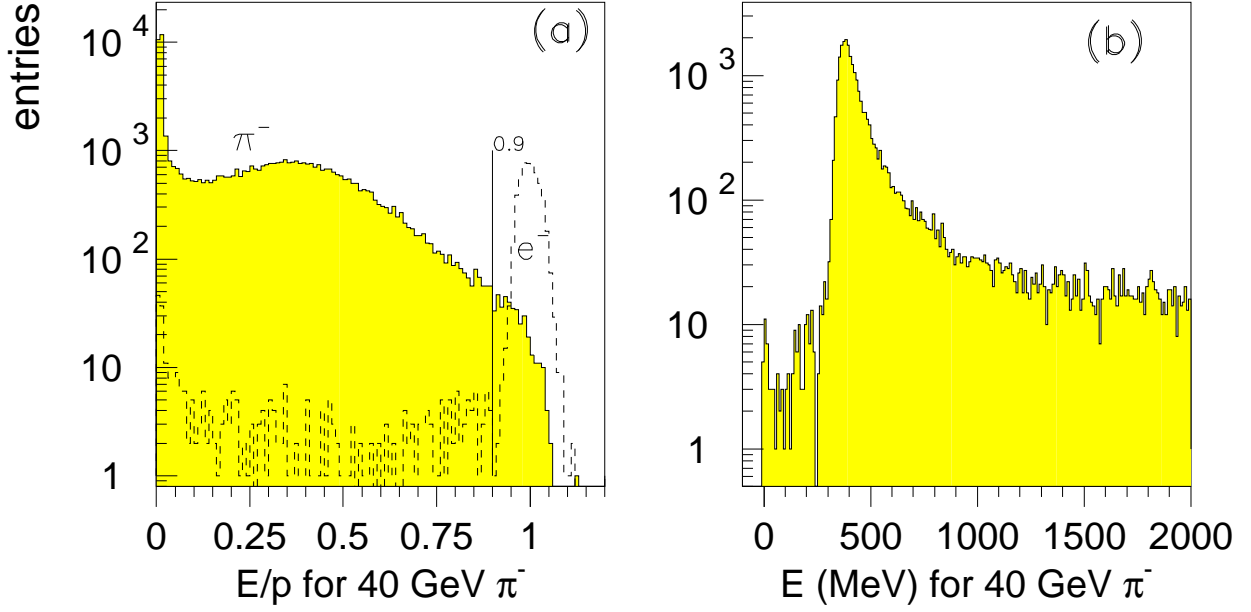


Figure 15: (a) E/p spectra for π^- (shaded) and e^- (dashed) at 40 GeV/c and (b) energy spectrum for π^- MIP peak. The energy sum is over the inner nine blocks, using only the in-time slice. The line at $E/p = 0.9$ defines 100% e^- acceptance.

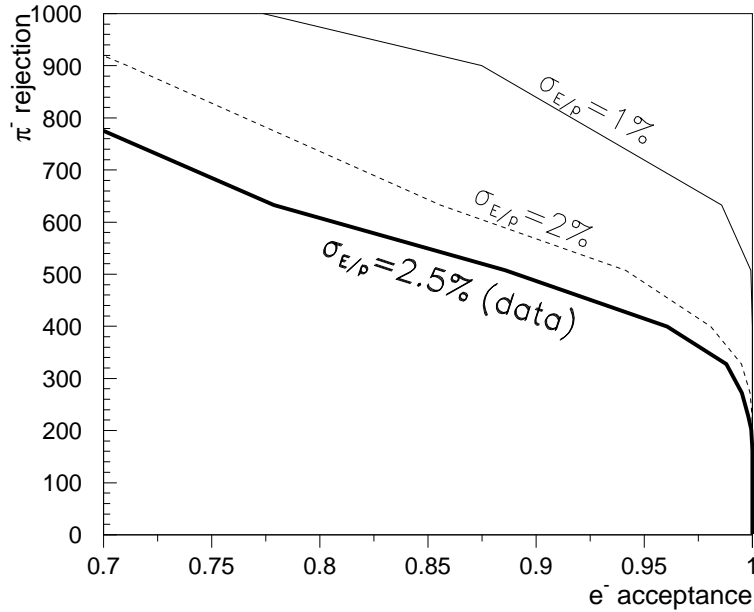


Figure 16: π^- rejection vs. e^- efficiency at 40 GeV/c. The thick solid line is from the data. The thin lines are extrapolations based on replacing the e^- E/p spectrum with Gaussians whose widths are shown in the figure.

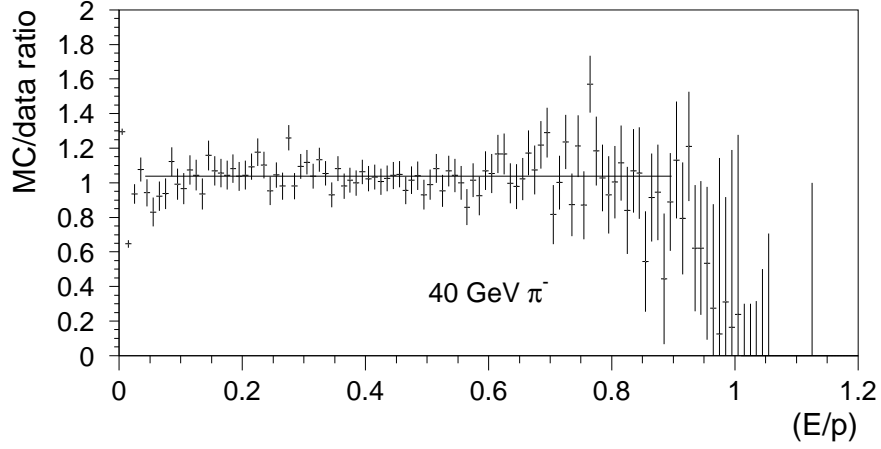


Figure 17: MC/data ratio for 40 GeV/c π^- . The MC program used GEANT/FLUKA for pion shower generation. The horizontal line is to guide the eye.

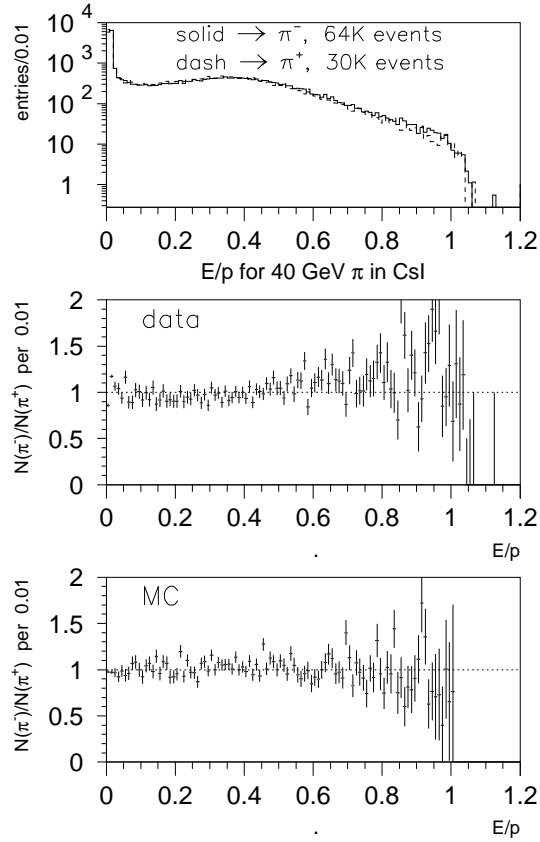


Figure 18: Comparison of π^- and π^+ response in CsI. The π^+ E/p spectrum was scaled to have the same area as the π^- E/p spectrum. The middle plot shows the ratio of the π^-/π^+ spectra as a function of E/p . The last plot is the π^-/π^+ ratio predicted by a GEANT based simulation.

5 Uniformity Measurement with Muons

To maintain good energy resolution, it is important that the CsI crystal response remains uniform along the length of each crystal. In the KTeV experiment, cosmic muons will be used to monitor the uniformity profiles of each crystal in the array. This is designed to help understand the resolution function, and to detect changes in the uniformity.

After the data were collected for electrons and pions, the calorimeter was rotated 90° about the vertical axis, so that the longitudinal axis of the crystals was perpendicular to the direction of the beam (Fig. 19). The collimators were closed and the magnets were tuned to create a muon halo from a 70 GeV/c π^- beam. Eight narrow scintillator paddles, with a spacing of 6.5 cm, were mounted behind the array. These were used in coincidence with a large scintillator paddle in front of the CsI to trigger on muons. The paddles were used offline to determine the muon hit position relative to the PMT-crystal interface. The average energy deposit from a muon through 5 cm of CsI is ~ 35 MeV, producing a signal of about 30 FADC counts in the lowest range of the DPMT. Each FADC distribution was fit with a Landau curve to extract the peak of the pulse height distribution.

Fig. 20a shows the response of the central block to transverse muons for one 6.5 cm position bin. The response in each position bin was determined by fitting the FADC distribution with a Landau curve. The uniformity of the central block is shown in Fig. 20b. The response varies by $\sim 4\%$ over the length of this crystal. The uniformities for all 25 crystals were measured in the same fashion as the central block.

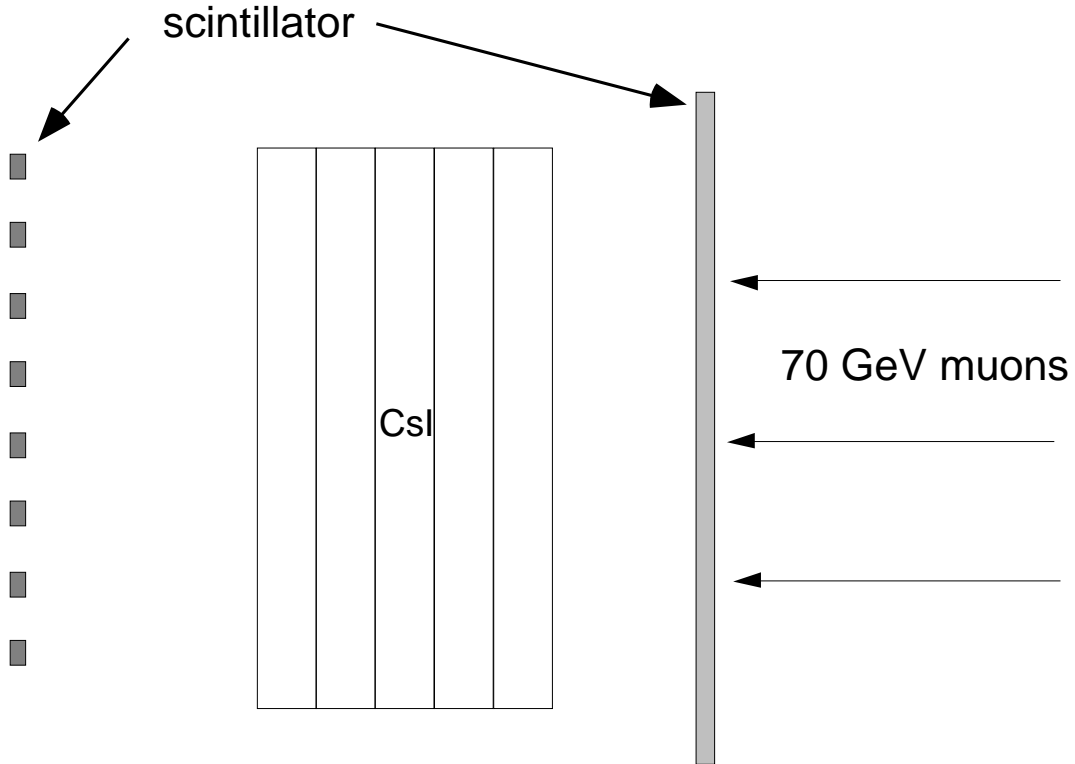


Figure 19: Setup used to measure the CsI non-uniformity with transverse muons in the X1 beam-line.

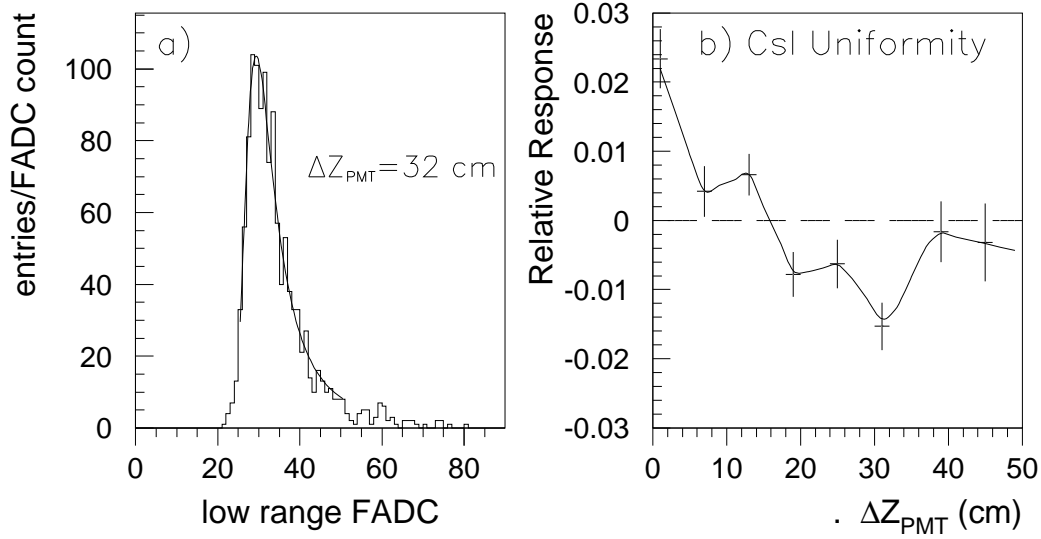


Figure 20: (a) CsI FADC for transverse muons. The peak at 30 counts corresponds to 30 MeV, and the curve is a Landau fit. Note that the muon signal is in the lowest range ($I/2$) of the DPMT. (b) The relative response (deviation from average) vs. distance from the PMT for the central block in the array. The curve is drawn to guide the eye.

6 CsI Simulation

This section describes the Monte-Carlo simulation used to predict the electron energy resolution and pion response of the CsI prototype calorimeter.

The first part of the simulation used GEANT [10] to generate the energy deposits in each crystal. Each incident beam particle (e , π , μ) was tracked from the exit of the last vacuum pipe window, which was about 25 meters upstream of the CsI array. The initial momentum and transverse position were selected from independent Gaussian distributions. The GEANT tracking upstream of the CsI included about 13 meters of air ($0.042 X_0$) and 5 mm of mylar windows on the Cerenkov counters ($0.017 X_0$). The 5- and 7-meter long Cerenkov counters were evacuated.

The measured non-uniformities in each of the CsI crystals (Sec. 5) were used as input to the Monte Carlo. The energy deposits determined by GEANT were recorded in 2 cm segments along the crystal axis and then weighted by the measured non-uniformity.

The second step involved multiplying the GEANT energy deposits by the measured number of photo-electrons per MeV to simulate the photo-statistics contribution ($\sim 0.2 - 0.3\%$) to the resolution function. The charge into the DPMT was obtained by multiplying N_{pe} by the PMT gain. A detailed simulation of the DPMT then converted the input charge Q into an exponent and mantissa.

7 Conclusion

We have successfully completed a test of the KTeV CsI calorimeter system at the CERN X1 beam-line. After accounting for the calculated beam dispersion, the *intrinsic* CsI resolutions were determined to be better than 1% for electrons with momenta ranging from 5–60 GeV/c. Comparing the calorimeter response to 40 GeV/c pion and electron beams, each with a 2.5% RMS momentum spread, a π^- rejection factor of $420 \pm 35(stat)$ was obtained with 95% e^- efficiency. A pion rejection factor of $720 \pm 75(stat)$ is obtained if the beam dispersion is ignored and a calorimeter resolution of 1% is assumed. Using beam muons transverse to the CsI array, the relative responses were determined to be better than 1% every 6.5 cm along the crystal axis.

We are grateful to the CERN staff for their hospitality, especially to Per Grafström for his guidance in using the X1 beam-line, and to Giles Barr for his coordination of the experiment. We would also like to acknowledge the support of the Fermilab Research Division EE Department, the Fermilab Physics Section, the DOE and the NSF. One of us (TN) would like to acknowledge support from the JSPS Fellowship for Japanese Junior Scientists.

References

- [1] B.Winstein, *A Pure CsI Calorimeter for the Study of Kaon Decays*, Heavy Scintillators for Scientific and Industrial Applications, (Edition Frontieres, 1993), p. 279.
- [2] A.Roodman, *Radiation Damage and Scintillation Uniformity in Pure CsI*, Heavy Scintillators for Scientific and Industrial Applications, (Edition Frontieres, 1993), p. 479.
- [3] R.J.Yarema et. al., *A Pipelined Multiranging Integrator and Encoder ASIC for Fast Digitization of Photomultiplier Tube Signals*, 2nd Annual Conference on Electronics for Future Colliders, Chestnut Ridge, New York, 1992.
- [4] R.J.Yarema et. al., *A Fast, Wide Range Charge Integrator and Encoder ASIC for Photomultiplier Tubes*, IEEE Trans. on Nuclear Science, Vol 4 (August 1993), pp. 750-752.
- [5] R.J.Yarema et. al., *A High Speed, Wide Dynamic Range Digitizer Circuit for Photomultiplier Tubes*, Presented at the 6'th Pisa Meeting on Advanced Detectors, (22-28 May, 1994) La Biodola, Isola d'Elba, Italy.
- [6] P.Grafström, *Short Introduction to the use of the X1 Beam*, SL/EA/PG/cnp (Mem.91-25), 12-Sep-1991.
- [7] K.L.Brown and F.C.Iselin, *Decay Turtle: A Computer Program for Simulating Charged Particle Beam Transport Systems, Including Decay Calculations*, CERN-74-2, (Feb, 1974).
- [8] Per Grafström, *private communication*.
- [9] H.Kobayashi et. al., *Pure CsI: New Fast Scintillator for γ Detectors*, pre-print KUNS-900, November 1987.
- [10] *GEANT Detector Description and Simulation Tool*, CERN Program Library Long Writeup W5013. Also see FLUKA references [2,3,4,5,6] within.